Check for updates

A nano-platform harnessing synergistic amino acid browning for biomedical applications†

Teh-Min Hu, [ID] * Jia-An Liang [ID] and Yi-Hua Chiang

Amino acids show promise as versatile biomolecules for creating a variety of functional biomaterials. Previously, we discovered a novel amino acid reaction, in which a single amino acid can form browning species in a simple solvent mixture comprising DMSO and acetone at room temperature. In the present study, we initially conducted a comprehensive analysis of 190 pairs of binary amino acids (*i.e.*, all the possible pairwise combinations out of 20 amino acids) and identified several surprising combinations that exhibited synergistic browning effects. Particularly, cysteine–lysine and cysteine–arginine pairs exhibited pronounced browning in DMSO/acetone cosolvent solutions. We hypothesize that the coloured species result from the formation of extended, hydrophobic molecules with highly conjugated systems, arising from extensive condensation reactions between amino acids. Subsequently, we aimed at developing a nano-platform based on this newly discovered amino acid reaction. We demonstrate that through a nanoprecipitation process (solvent-shifting), spherical nanoparticles with sizes ranging from 100 to 200 nm can be produced, in the presence of ferric ions added to the water phase. Through systematic optimization and comprehensive characterization, the final product is a zwitterionic, charge-reversible nanoparticle featuring three functional groups on its surface: carboxylates, amines, and thiols. Furthermore, it possesses mild antioxidant activity, making it a new type of nano-antioxidant. Finally, we present preliminary results highlighting the potential of using this new nanomaterial as a delivery system for polynucleotides. In conclusion, the paper introduces a novel class of amino acid-derived nanoparticles with significant promise for future biomedical applications.

Introduction

Throughout the global pandemic, we have witnessed and actively engaged in the remarkable accomplishment of nano-drug delivery systems. Notably, the advent of lipid-nanoparticle-based mRNA vaccines has marked a pivotal milestone in the battle against COVID-19, offering tangible benefits to the worldwide population. One of the cornerstones of this achievement lies in extensive, decade-long research on lipid molecules as the fundamental constituents of drug-encapsulating nano-vehicles.[1–4] Recently, amino-acid derivatives have been shown to be promising alternatives to lipids for constructing nano-drug carriers.[5–7] A broad spectrum of nano- and microstructures can be directly formed through self-assembly of 1 to 3 amino acids with prior structural modifications.[7–13] This presents significant opportunities for the design and preparation of novel formulations for drug delivery.
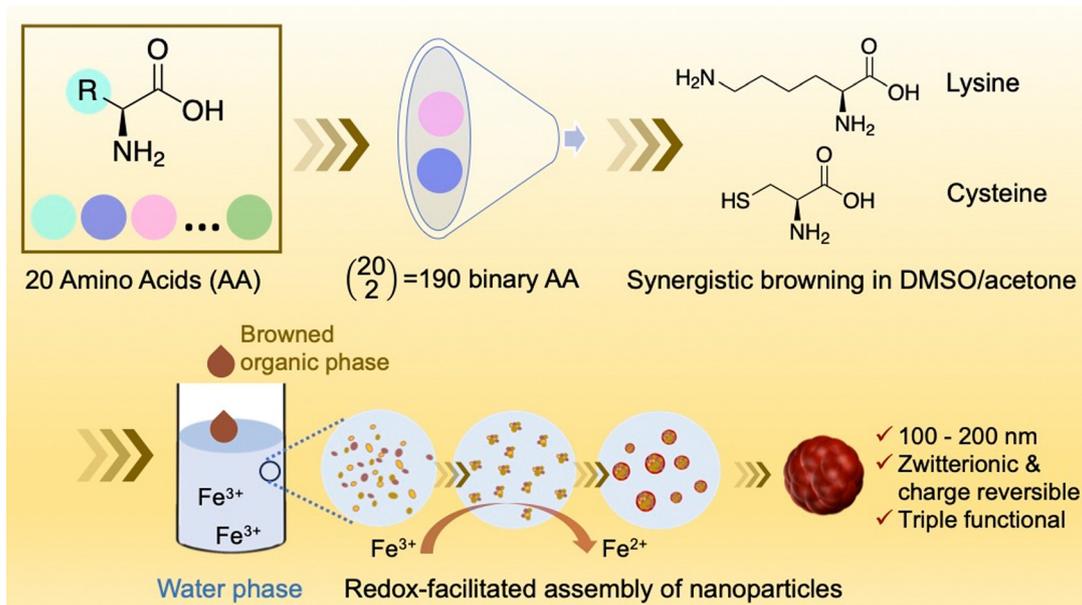
This present study builds upon unexpected findings from our previous research. Our initial focus was on the development of organosilica–protein hydrogels for drug delivery.[14–16] During certain stages of this work, we made attempts to remove the organosilica structure from the freeze-dried protein hydrogel by immersing the gel bodies in a combination of DMSO and acetone. Surprisingly, this led to colour transformation, changing the white gel into a brown gel.[16] Intrigued by this phenomenon, we embarked on a series of experiments and made the discovery that this browning reaction is a general occurrence, extending its reach to pure proteins and even amino acids.[16] In our subsequent study,[17] we delved into the potential mechanism behind this novel amino acid browning reaction, which occurs spontaneously at room temperature, requiring only three components: tryptophan, DMSO, and acetone. We demonstrated that the initial self-aldol condensation of acetone, catalysed by tryptophan acting as an organocatalyst in our solvent system, may trigger further molecular condensations, ultimately leading to the formation of extended molecules with sufficient conjugated systems capable of absorbing visible light. Furthermore, the hydrophobic properties of the light-absorbing species enable them to form nanoparticles in water, with bovine serum albumin serving as a stabilizing agent.[17]

In our present study, we expand upon the three-component system, exploring the possibility of introducing an additional

Department of Pharmacy, College of Pharmaceutical Sciences, National Yang Ming Chiao Tung University, 112304 Taipei, Taiwan. E-mail: tehmin@nycu.edu.tw

† Electronic supplementary information (ESI) available. See DOI: https://doi.org/10.1039/d4tb00529e

6410 | *J. Mater. Chem. B*, 2024, **12**, 6410–6423

This journal is © The Royal Society of Chemistry 2024

Scheme 1 Schematic representation illustrating the process leading to the development of a nano-platform based on the synergistic browning of dual amino acids in the DMSO/acetone cosolvent system.

amino acid into the existing triad system. Our initial investigation aimed to determine whether this expansion could enhance the chemical diversity of the recently discovered amino acid reaction. Through an initial screening of all possible 190 pairwise amino acid combinations of the 20 common amino acids, we identified several combinations that exhibited synergistic browning effects. We focused our attention on the cysteine–lysine pair due to its remarkable nanoparticle-forming capabilities. After systematic and comprehensive characterization and optimization, we successfully engineered a nano-platform (Scheme 1) that produces nanoparticles with triple functional groups derived from dual amino acids. These nanoparticles exhibit zwitterionic and pH-dependent charge reversal capability and possess mild antioxidant activity. Notably, we have also demonstrated the feasibility of using this new nanomaterial as an effective nanocarrier for polynucleotide delivery.

Results

Initial screening of 190 pairwise amino acid combinations

We first conducted a rapid pilot screening to investigate the solvent mediated browning reaction in solutions containing two amino acids. The total number of binary combinations is 190 for 20 common amino acids (Scheme 1). The binary amino acid systems were prepared in DMSO/acetone (9/1) at equal amino acid concentrations (2.5 mg mL^{-1}). After placing the solution at room temperature for 48 h without thermal and mechanical perturbations, the appearance of all the solutions was compared in Fig. S1 (ESI†). The collective picture is consistent with our previous study that tryptophan (**W**) is the amino acid with the highest browning potential. The addition of other amino acids to tryptophan would either enhance,

inhibit, or have no effect on the browning of tryptophan. We are currently working on gaining better understanding about the tryptophan reaction in separate studies. The study described herein, however, starts from the surprising finding that the cysteine–lysine (**C**–**K**) and cysteine–arginine (**C**–**R**) pairs show a synergistic browning effect, given that the three amino acids, when present alone, show no or weak browning potential.

Synergistic browning of the C–K and C–R pairs

The cysteine–lysine (**C**–**K**) and cysteine–arginine (**C**–**R**) combinations were further investigated to demonstrate the synergistic browning effect (Fig. 1). For the **C**–**K** pair, the degree of browning increased with increasing concentrations of lysine in the presence of cysteine at a fixed concentration (Fig. 1A). The UV-vis spectra show the characteristic peak of browning products at 320 nm (Fig. 1B). The increase of absorption intensity in the visible light range corresponds to the change in brown colour intensity. Accordingly, the absorbance at 420 nm was used to compare the degree of browning in different solutions (Fig. 1C). Clearly, the data reveal significant synergism for the **C**–**K** combinations, compared with lysine alone. Similarly, the **C**–**R** combination also led to synergistic browning: the extent of browning increases with increasing arginine concentrations and reaction time (Fig. 1D). However, the **C**–**R** synergism is more dramatic (Fig. 1E), given that each amino acid alone did not brown in the reaction system (Fig. 1F).

Cysteine concentration-dependent synergism

The role of cysteine in facilitating the browning effect of lysine and arginine was further illustrated by performing reactions with varying cysteine concentrations in the presence of the other amino acid at a fixed concentration. Fig. S2 (ESI†) shows the concentration-dependent effect of cysteine in the binary
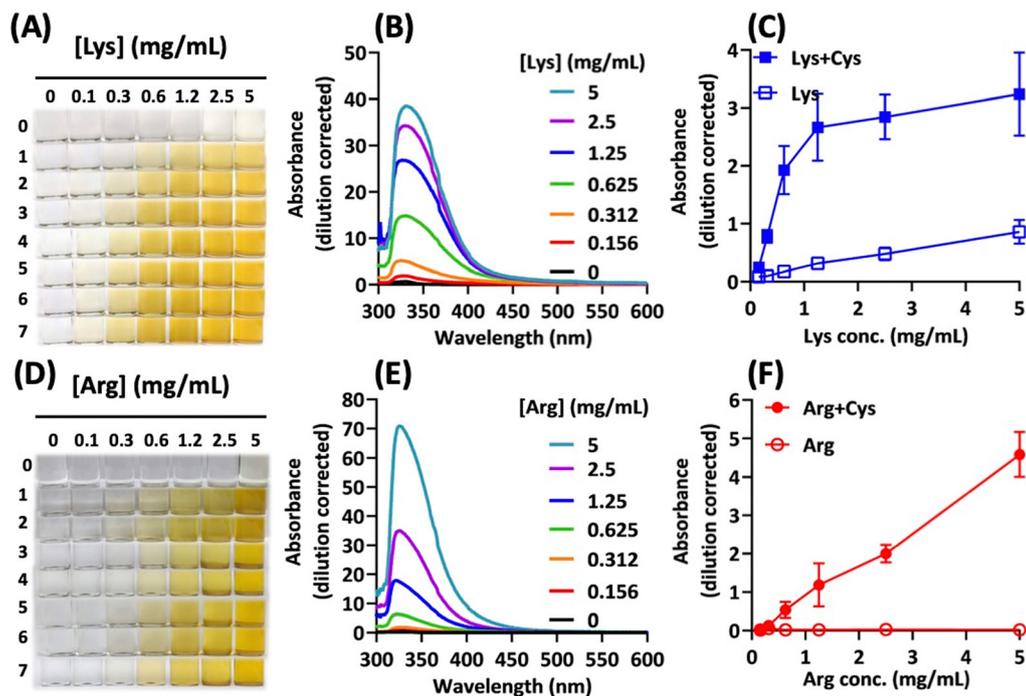
Fig. 1   Synergistic browning effect of lysine–cysteine and arginine–cysteine pairs. (A) Appearance of solution containing cysteine (1.25 mg mL^{-1}) and increasing concentrations of lysine (0 to 5 mg mL^{-1}) in DMSO/acetone (9/1), as shown from the initial time to day 7. (B) Dilution-adjusted UV-vis spectra of lysine–cysteine solutions at day 7. (C) Comparison of dilution-adjusted absorbance at 420 nm for lysine–cysteine combination solutions and lysine alone, at different lysine concentrations. (D)–(F) Counterparts of (A)–(C) for the arginine–cysteine pair.

amino acid systems. For the **C**–**K** system, the observed synergism is dependent on cysteine concentrations in a capacity limited manner. However, the **C**–**R** system shows biphasic synergism, where peak synergism occurred at an intermediate cysteine concentration.

Rationales for nanoparticle synthesis

In this study, we chose the **C**–**K** system to investigate the feasibility of preparing nanomaterials from the browning products of binary amino acids, based on the following considerations. First, like the tryptophan system,[17] our HPLC analysis shows multiple peaks with significantly extended retention times on a reverse-phase chromatographic system (Fig. S3, ESI†), indicating the hydrophobic nature of the browning products. This is further supported by the formation of brown precipitates upon mixing the organic browning solution with water. Second, we hypothesize that adding metal ions to the precipitation system would increase the physicochemical versatility in producing nanosized functional materials. This was inspired by the fact that metal complexation with electron-rich organic molecules, *e.g.*, polyphenol, could generate self-assembled materials of various forms for a broad range of applications.[18–23]

Ferric ions facilitate nanoprecipitation

In the initial tests, we showed that a ferric salt, but not ferrous and zinc salts, could cause marked colour transformation in the browned solution of cysteine–lysine (Fig. S4, ESI†). Upon adding the solvent solution of browned amino acids to an aqueous solution containing ferric chloride, the colour of the final mixing solution immediately changes from light brown to dark bluish-green or dark brown, depending on the concentration of the ferric salt. The next result (Fig. 2A) indicates that the green colour transformation is the strongest at an optimal concentration of ferric ions, Fe(III). For example, at a mixing ratio of 2 : 8 (v/v; browned solvent to Fe(III)-containing aqueous solution), the maximal colour intensity occurs at 23.1 mM Fe(III) (Fig. 2B), which corresponds to maximal absorption at 650 nm. At higher mixing ratios, Fig. 2C shows a right shift in peak colour changes, where the highest intensity and peak absorption occur at higher Fe(III) concentrations. Apparently, the solvent properties of the mixed solution also affect the interaction of Fe(III) with browned amino acid species. Moreover, as shown in Fig. S5 (ESI†), the degree of browning correlates with green colour intensity, suggesting stoichiometric interaction between Fe(III) and browned amino acid species.

Further optimization of the nanoprecipitation conditions

In the following experiments, the concentrations of cysteine and lysine in the binary reaction system were varied to select a better combination for interacting with Fe(III) across various concentrations and formation of nanoparticles. Fig. S6 (ESI†) shows that the combination of 10 mg mL^{-1} cysteine and 5 mg mL^{-1} lysine in the browning solvent would generate the most intensive colour formation upon mixing with Fe(III) and lead to the formation of more homogeneous particles with a hydrodynamic
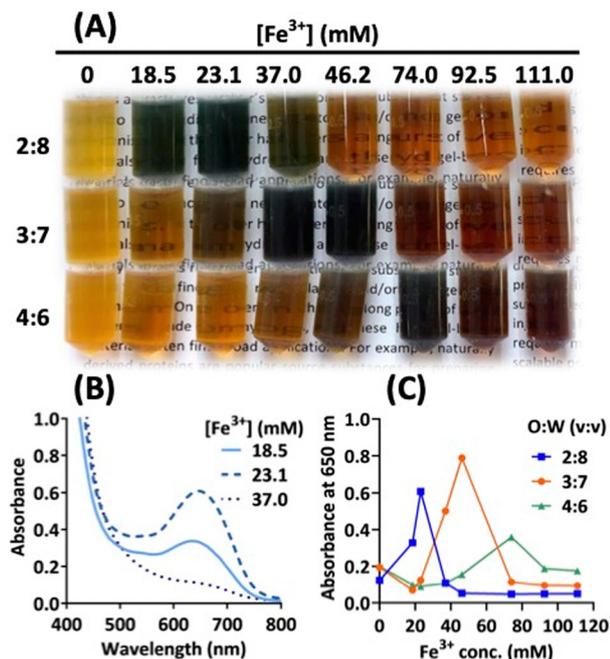
Fig. 2 Effect of ferric ions on brown-to-green colour transformation by mixing amino acid browning solutions in DMSO/acetone with aqueous ferric chloride solutions. (A) Visual images of mixing solutions captured after 4 h at different organic (o) phase to water (w) phase ratios (o/w = 2 : 8, 3 : 7, 4 : 6). (B) UV-vis spectra of the green colour solutions obtained for the O/W ratio at 2 : 8 (C) Absorbance at 650 nm plotted against ferric ion concentrations. Reaction conditions for the organic phase: [cysteine] = 10 mg mL^{-1}; [lysine] = 2.5 mg mL^{-1}; reaction time = 7 days; room temperature.

diameter of about 200 nm and PDI close to 0.1 (Fig. S7, ESI†). While the optimal **C–K** combination (*i.e.*, **C** = 10 mg mL^{-1}, **K** = 5 mg mL^{-1}) demonstrated a relatively stable hydrodynamic size and polydispersity index (PDI) across varying ferric ion concentrations during nanoprecipitation (Fig. S7, ESI†), particles collected after centrifugation exhibited tendencies toward aggregation at high ferric ion concentrations (Fig. S8, ESI†).

Colour transformation in the aging process

Up to now, we have shown that the solvent browned cysteine–lysine could potentially form ferric complexation products having potential for producing nanoparticles after solvent shifting in water. The logical next step is to collect nanoparticles from the solution mixture. During the particle collecting procedure, we observed the following phenomena. (1) The colour of the solution slowly and continuously changed over time, from initial green to reddish brown after 7 days (Fig. 3). The visible spectra reveal the details of the dynamic colour change: in the first 24 h, the characteristic peak around 620–650 nm (corresponding to red-light absorption) rapidly grew in intensity (Fig. 3A). In the following days, the peak intensity at 650 nm slowly declined, accompanied by the formation of a new absorption peak around 500 nm (blue- or green-light absorption) (Fig. 3B). (2) The collected particles (through dialysis) appear reddish brown and show only one characteristic peak at 500 nm; moreover, the quantity of

collectable particles increased over time (Fig. 3C). These findings suggest that an aging process is needed to convert the initial green ferric complexes to reddish brown species capable of self-assembling in aqueous media. Accordingly, the formation of nanoparticles in the reaction system is a kinetically controlled process. At room temperature, it takes at least 7 days to reach near-completion.

Optimizing the aging process and particle collection

To facilitate the aging process, we elevated the reaction temperature. Fig. 3D shows that the increase in temperature significantly accelerated the aging process, as indicated by a more rapid rise in absorbance at 500 nm over time at higher aging temperatures. After 24 hours of aging, particles were purified and collected through dialysis. Fig. 3E shows the UV-vis spectra of the collected particle solutions. Clearly, higher aging temperatures resulted in more concentrated nanoparticle solutions.

Size and morphology of the final nanoparticle product

The final solutions were subjected to particle size measurements using dynamic light scattering. The results are shown in Fig. S9 (ESI†). Overall, raising the aging temperature up to 60 °C not only significantly facilitates the preparation procedure, but also produces smaller and more homogeneous nanoparticles (Fig. S9A, ESI†). Furthermore, the collected particles show stable particle sizes under storage conditions, especially for preparations with higher aging temperatures (Fig. S9B, C and D, ESI†). The electron microscopic images reveal spherical particles (mostly 100–200 nm) with a solid core and granular raspberry-like surface (Fig. 4).

Electrochemical properties

We assessed the electrochemical properties of the nanoparticles across a wide range of solution pH values. In Fig. 5A, the freshly prepared nanoparticle solution (with an initial acidic pH of 3.0) exhibits a zeta potential of approximately +30 mV. As we adjusted the pH of the particle solution by incrementally adding a sodium hydroxide solution (0.1 N), the zeta potential decreased sharply. Particularly, the zero crossing of the zeta potential occurs around pH 4.5, followed by a continuous decline to reach a highly negative zeta potential in the range of −40 to −50 mV at pH values exceeding 9.

Fig. 5B and C present hydrodynamic size and polydispersity index (PDI) measurements at these pH values, revealing a shaded region indicating substantial particle aggregation and size deviations. This region corresponds to the pH range of 3.5 to 5.5, where the absolute zeta potential of the particles falls below 20 mV. These findings are consistent with the electrostatic properties of charged particles. Importantly, the results unveil a zwitterionic nanoparticle with an isoelectric point (pI) of 4.3.

EDS, FTIR, and XPS analyses

The final nanoparticles were subjected to energy-dispersive X-ray spectroscopy (EDS) analysis, to provide an initial
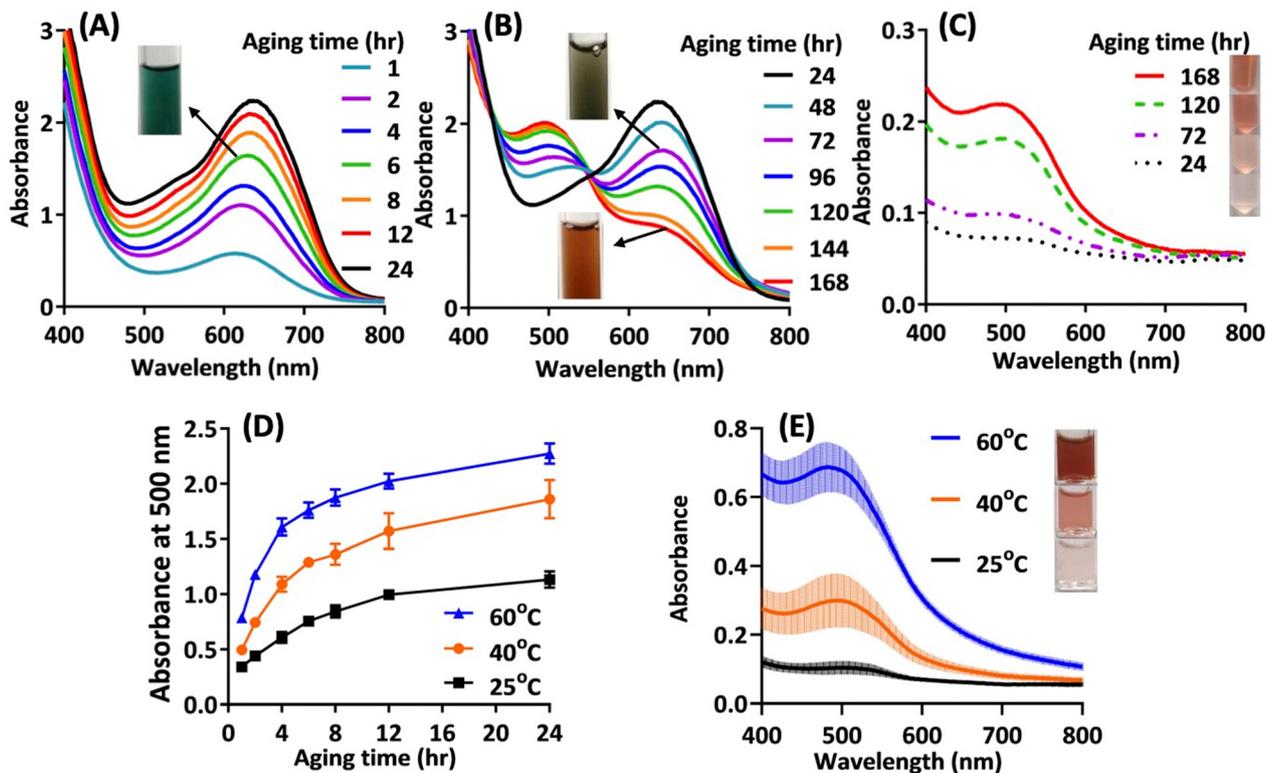
Fig. 3 Dynamic colour changes and nanoparticle formation upon ferric complexation of solvent-browned cysteine−lysine. (A) Rapid growth of the UV-vis spectra within the first 24 h of aging at 25 °C, highlighting the initial green colour. (B) Dynamic green-to-red colour change observed after the second day of aging at 25 °C, accompanied by spectral changes characterized by a decrease in peak intensity at 650 nm and an increase in intensity at 500 nm. (C) UV-vis spectra and the corresponding visual images of finally purified nanoparticle solutions obtained by subjecting aged solutions with different aging times (24, 72, 120, and 168 h; 25 °C) to dialysis. (D) Accelerated maturation of nanoparticles at elevated aging temperatures. (E) UV-vis spectra and photo images of collected particle solutions. See Experimental for detailed preparation conditions.
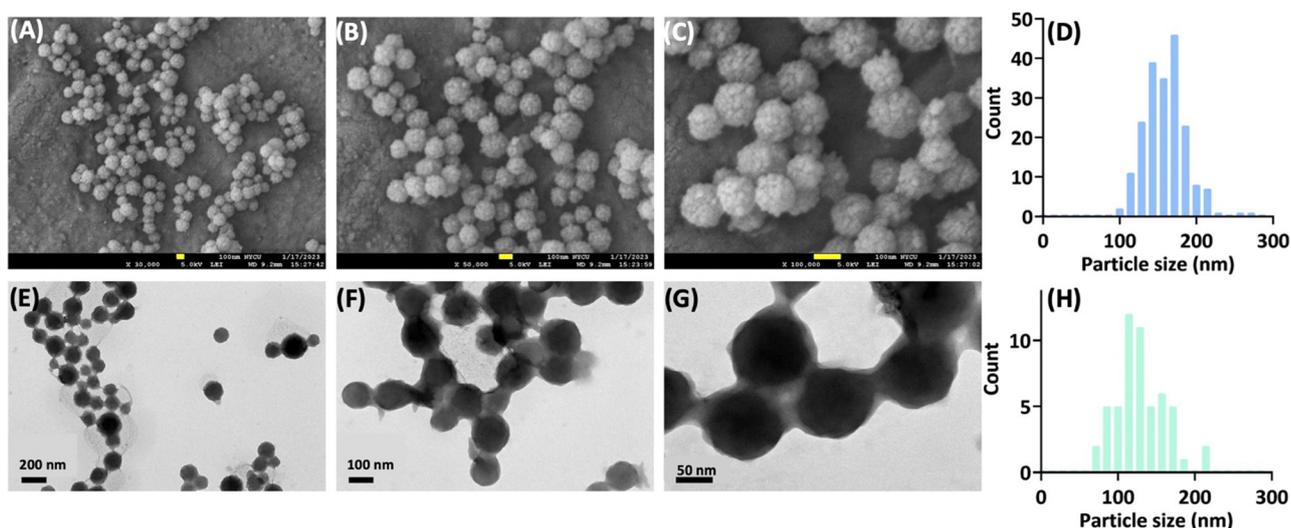

Fig. 4 Characterization of nanoparticle morphology. (A)−(C) SEM images at different magnifications (yellow bar = 100 nm). (D) Size distribution for the SEM image A. (E)−(G) TEM images at different magnifications. (H) Size distribution for the TEM image E.

assessment of the sample's elemental composition. The result (Fig. S10, ESI†) revealed that carbon (C) constitutes the highest proportion at 76.5%, followed by oxygen (O) at 16.8%. A substantial number of sulphur (S) atoms were observed at 5.8%.
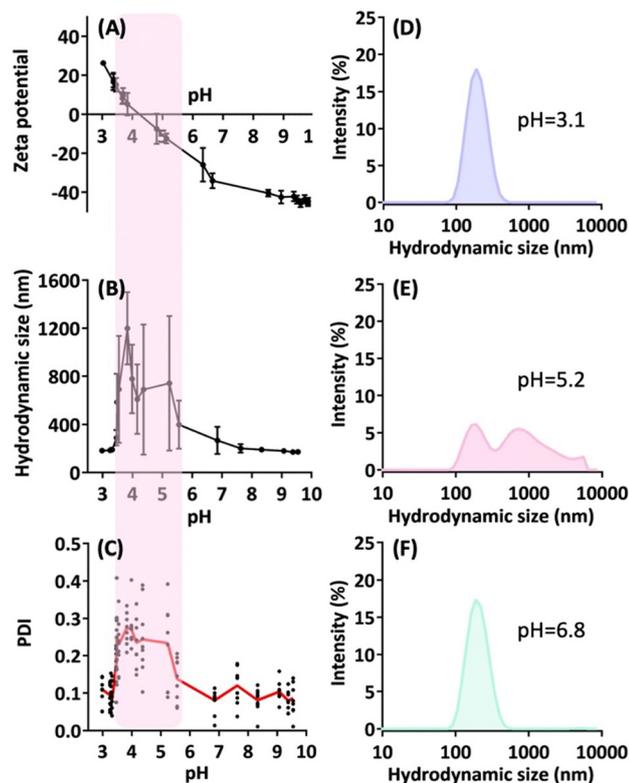
6414 | *J. Mater. Chem. B*, 2024, **12**, 6410–6423

This journal is © The Royal Society of Chemistry 2024

Fig. 5 Characterization of surface charges, hydrodynamic sizes, and size distribution at various pH levels. (A) Zeta potential. (B) Hydrodynamic size. (C) Polydispersity index. The zeta potential and hydrodynamic data represent the mean ± standard deviation (S.D.) of three independent experiments, plotted against mean pH values. The shading in (A)–(C) indicates the region of particle instability. (D)–(F). Size distribution profiles (averaged) for preparations at mean pH = 3.1 (D), 5.2 (E), and 6.8 (F).

Notably, a trace amount of iron (Fe) at about 1% was also detected. Nitrogen (N) remained undetectable due to EDS limitations, as it is not well-suited for nitrogen detection.

The molecular structure within the particle matrix was further examined using Fourier transform infrared (FTIR). Fig. S11 (ESI†) compares the FTIR spectra of lysine, cysteine, and the nanoparticles. The data reveal that the nanoparticle spectrum exhibits the typical vibrational characteristics associated with amino acids, such as stretching vibration of C=O (around 1550–1650 cm^{-1}) and N–H stretching (around 3000–3400 cm^{-1}), but with significant modifications in the fingerprint region (500–1500 cm^{-1}). This region is characterized by broadening peaks with reduced resolution, likely a result of complex vibration interactions involving heterogeneous molecular assembly within the confined particle matrix. Despite these changes, the characteristic peak at 2550 cm^{-1} representing the S–H stretching vibration of cysteine[24,25] has been notably altered in the nanoparticle sample. This characteristic peak has disappeared, and the surrounding region is depressed. Furthermore, the absence of the N–H stretching at around 2080–2100 cm^{-1} for the two amino acid salts (assigned to the protonated amine in the hydrochloride salt[24]) suggests that the chemistry involving the amine group has also been significantly altered in the final product.

The elemental composition and chemical states of the nanoparticle surface were analysed by X-ray photoelectron spectroscopy (XPS). The survey scan spectrum (Fig. 6A) indicates that the major surface elements are carbon (C) at 72.8%, followed by oxygen (O) at 13.8%. Besides, substantial amounts of sulphur (S) and nitrogen (N) are present, each comprising approximately 6% of the surface composition.

The C 1s spectrum (Fig. 6B) reveals that C–C/C–H species are the predominant components, constituting 73.9%. Furthermore, carbonyl (C=O) and carboxylate (O–C=O) species are also detected on the surface, making up 6.7% and 2.5%, respectively. The remaining 16.9% is attributed to other potential carbon species (C–O/C–S/R–C=N/R–NH$_2$). Notably, the presence of R–C=N and R–NH$_2$ was confirmed by the N 1s spectrum (Fig. 6C), while the presence of C–S was verified by the S 2p spectrum (Fig. 6E). The detection of surface R–NH$_2$ groups and their protonated state in Fig. 6C indicates the potential for positive surface charges.

Overall, XPS analysis provides several insights into the browning reaction and the observed nanoparticle properties. First, based on the C 1s (Fig. 6B), N 1s (Fig. 6C), and O 1s (Fig. 6D) spectra, it is evident that carboxylate and amino groups of some of the amino acids persist on the particle surface, contributing to the nanoparticles' zwitterionic nature, as illustrated in Fig. 5, depicting pH-dependent charge reversal. Second, the detection of a C=N bond suggests that the solvent-mediated browning of amino acids also involves the condensation of amines with carbonyl compounds (ketones or aldehydes) or carboxylates to form a Schiff base (imine), a significant reaction identified in the Maillard reaction.[26] Finally, the analysis of sulphur 2p spectra points to significant oxidative reactions taking place in the browning system, leading to the formation of disulphide bonds; however, most sulphur species observed on the particle surface remains in its original, unoxidized thiol group (C–SH), *i.e.*, the C–S (s2p3) peak (Fig. 6E).

Biomedical applications

After establishing a new nanoparticle platform based on the synergistic browning reaction of amino acids, our next objective was to identify its potential applications in biomedicine and drug delivery. Therefore, we conducted several preliminary studies to underscore its promise. To begin, we proposed that the nanoparticle may possess antioxidative capabilities due to the presence of cysteine's thiol group and brown species with extended and highly conjugated double bonds. As shown in Fig. 7A and B, the nanoparticle exhibits concentration-dependent free radical scavenging activity in the DPPH and ABTS assays. Moreover, the antioxidant capacity was further confirmed by the FRAP assay (Fig. 7C), revealing a reducing power one-tenth that of ascorbic acid, equivalent to 0.1 mg ascorbic acid/mg nanoparticle (Fig. 7D). Thus, the nanoparticle inherently functions as a mild antioxidant. This nanoparticle-based antioxidant warrants further investigation as a novel form of gentle nano-antioxidant, which could potentially mitigate the toxicity associated with traditional, double-edged small molecular antioxidants.
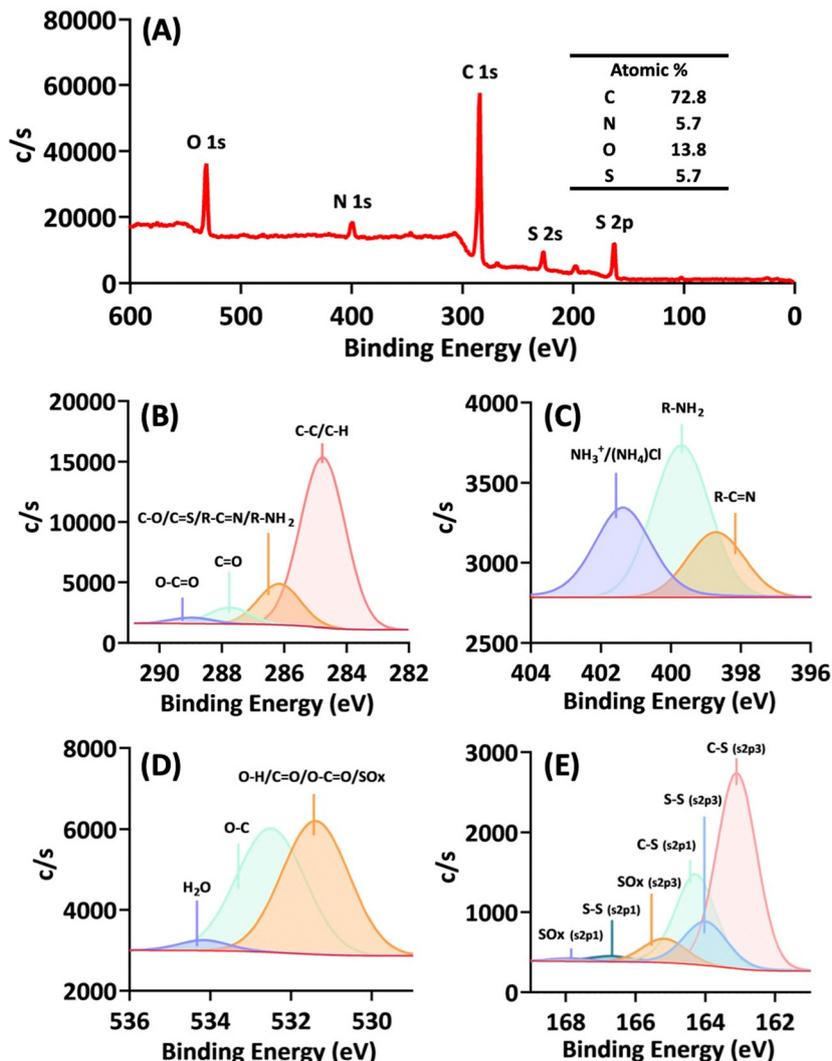
This journal is © The Royal Society of Chemistry 2024

J. Mater. Chem. B, 2024, **12**, 6410–6423 | **6415**

Fig. 6 X-ray photoelectron spectroscopy (XPS) analysis of the nanoparticles. (A) Survey scan spectrum. (B) C 1s spectrum. (C) N 1s spectrum. (D) O 1s spectrum. (E) S 2p spectrum.

The nanoparticle is zwitterionic, with positive and negative surface charges derived from the carboxylate and amine groups present in the initial amino acids. Besides, thiol groups from cysteine are also present on the particle's surface. Accordingly, our nanoparticle can be regarded as a triple-functional nanoparticle, holding the potential for versatile applications in nano-drug delivery. Specifically, its zwitterionic characteristic offers several advantages. First, it can enhance nanoparticle stability in biological fluids by reducing interactions with biomacromolecules.[27–30] Second, its pH-dependent charge-switching properties can be harnessed to control the loading and release of a variety of drugs or therapeutic macromolecules.[31–33] For instance, the nanoparticle can be used in the preparation of delivery systems for DNA or RNA-based medicines or vaccines, using charge interactions under suitable pH conditions.

To demonstrate this feasibility, we investigated the interaction between the nanoparticle and G3139 (oblimersen), an 18mer phosphorothioate oligonucleotide.[34] The results indicate that the particle efficiently formed nanocomplexes with G3139 in a concentration-dependent manner, achieving a maximal entrapment efficiency of about 90% (Fig. 8A). Furthermore, the particle sizes and size distributions remained mostly unaltered after nucleotide complexation (Fig. 8B). This property holds promises for the formulation of nucleic acid-based vaccines, potentially offering two advantages: stabilizing the nucleic acid during storage and facilitating uptake by immune cells at the injection site. Importantly, the nanoparticle exhibited no cytotoxicity at concentrations below 0.1 mg mL^{-1} (Fig. S12, ESI†).

Discussion

In this paper, we present a novel approach to harness amino acid chemistry for the preparation of functional nanoparticles, focusing on the lysine/cysteine system. While the reaction mechanism of the solvent-mediated browning of dual amino acids has yet to be fully characterized in separate studies, our previous investigation into the single tryptophan system

6416 | *J. Mater. Chem. B*, 2024, **12**, 6410–6423

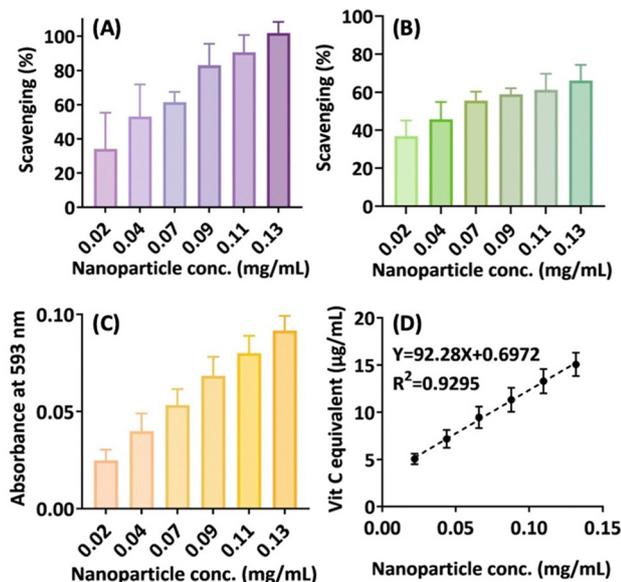This journal is © The Royal Society of Chemistry 2024

Fig. 7 Antioxidative activities of the nanoparticle preparation. (A) DPPH assay. (B) ABTS assay. (C) FRAP assay. (D) Estimated vitamin C equivalent concentrations.
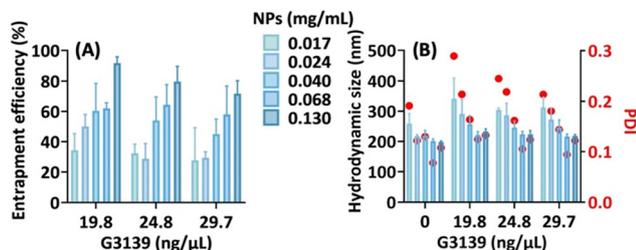

Fig. 8 The potential of nanoparticles (NPs) as nanocarriers for oligonucleotides. (A) Entrapment efficiency of G3139 (an 18-mer oligonucleotide). (B) Hydrodynamic sizes and polydispersity index (PDI) of the NP-G3139 complexes.

provides some initial insights.[17] In contrast to the significant browning observed in the tryptophan-alone system, lysine alone exhibits minimal browning, and cysteine shows no browning at all.[16,17] However, the current study demonstrates that the combination of lysine and cysteine within the same solvent system produces a browning effect comparable to that of tryptophan alone. In addition to the visual evidence provided by colour formation, our HPLC-DAD analysis allows us to illustrate the reactivity of the dual amino acid system, confirming the synergistic effect between lysine and cysteine in terms of the abundance of chemical species generated from the reaction (Fig. 9 and Fig. S13, ESI†).

Some specific observations are highlighted below. First, a major chromatographic peak with a retention time of about 28 min is identified as mesityl oxide (the structure is shown in Fig. 9F), which has been shown in our recent study to be a significant reactive intermediate formed through self-aldol condensation catalysed by amino acids.[17] We propose that

amino acid-mediated organocatalysis leads to the formation of reactive ketone or aldehyde species such as mesityl oxide, which, in turn, trigger subsequent condensation reactions with the amino groups present in amino acids.[17]

Secondly, it is worth noting that in the lysine–cysteine system, mesityl oxide formation is catalysed by lysine, but not by cysteine (Fig. 9D and E). These findings align with the browning effect observed in reactions involving either lysine or cysteine alone. Interestingly, when cysteine is absent, lysine alone induces a slight browning effect, despite producing a significant amount of mesityl oxide. This suggests the limited formation of pigmented species within the lysine-only system. However, in the mixed system, cysteine appears to serve as an additional reactant for mesityl oxide and its associated species, initially formed from lysine-catalysed aldol condensation. This phenomenon may potentially contribute to enhanced reactivity, as suggested by the extensive formation of new chemical species observed in the HPLC chromatogram (Fig. 9F).

Thirdly, it remains both important and intriguing to pinpoint the newly formed chemical species within the reaction system, particularly those contributing significantly to the development of brown pigments. However, this task has proven challenging in reactions involving traditional Maillard reactions.[35] Melanoidins, high-molecular-weight polymer-like molecules with molecular weights ranging from 1000 to 2000, are widely presumed to be the primary contributors to the brown coloration in common Maillard reaction systems.[35] Nonetheless, melanoidins remain enigmatic compounds that have yet to be fully identified, despite over a century of exploration into the Maillard reaction. Instead, research efforts on traditional Maillard reaction studies are focused on the meticulous isolation and identification of novel pigments, which typically consist of precisely defined small molecules.[36–40] Interestingly, these small molecular pigments often exhibit various colours, such as red, blue, and yellow, but they are usually not brown.[41–43]

Moreover, due to their extremely low abundance and the absence of characteristic absorption maxima in the visible light region (380–780 nm) in brown solutions, it has been hypothesized that the overall colour appearance results from a combination of different chromophores.[35,44,45] In our reaction system, preliminary HPLC-DAD analysis has revealed the diversity of chemical species formed, as exemplified by the UV-vis spectra (Fig. S14, ESI†). These results are expected to guide subsequent studies aimed at dissecting the reaction mechanism and identifying the specific products formed in this novel browning reaction.

Finally, in contrast to tryptophan, lysine and cysteine lack aromatic systems; hence, a more extensive reaction is necessary to generate colour-forming species, typically containing a high number of conjugated systems, particularly when aromatic rings are formed and coupled.[35,40] We speculate that cysteine may augment the colour-forming process through its thiol group, potentially involving a redox reaction. This hypothesis is supported by the observation that cystine, the oxidized form of cysteine, did not enhance the colour formation of lysine (Fig. S15, ESI†).
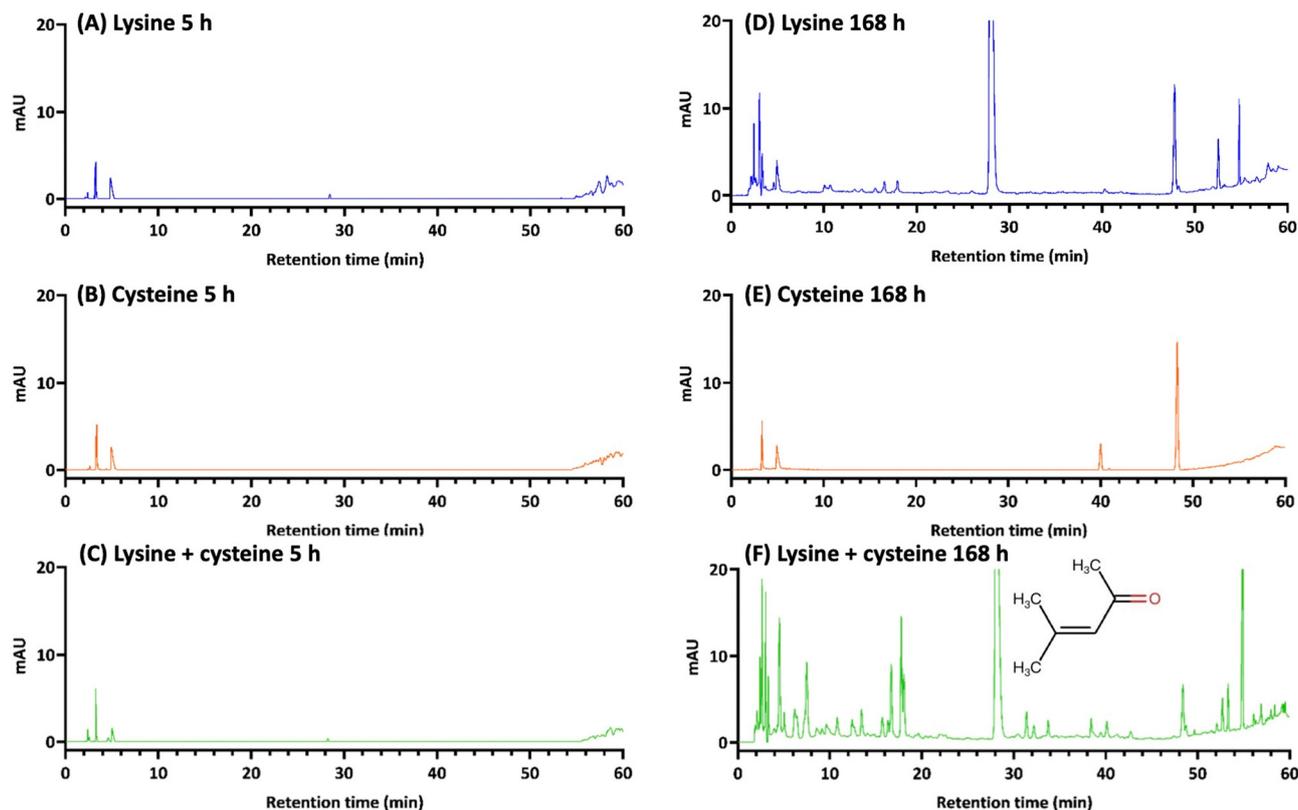
This journal is © The Royal Society of Chemistry 2024

J. Mater. Chem. B, 2024, 12, 6410–6423 | 6417

Fig. 9 HPLC chromatograms detected at 320 nm for amino acid solutions (1.25 mg mL^{-1}) reacting in DMSO/acetone (9/1 v/v) for 5 h (left panel; A–C) and 168 h (right panel; D–F). The major peak observed at 28 min was identified as mesityl oxide (C$_6$H$_{10}$O), with its structure shown.

Assembly of amino acids in aqueous environments often requires chemical derivations, involving the attachment of specifically designed moieties (usually hydrophobic) to the existing structure of amino acids. This modification facilitates the self-assembly process in water.[7–13] In this study, we demonstrate that the DMSO/acetone-mediated browning of dual amino acid mixtures could produce hydrophobic species with self-assembly properties in water. Our study reveals that the addition of ferric ions to the aqueous phase before solvent shifting can produce nanoparticle colloids with robust physical stability. Interestingly, the chemical processes persist beyond nanoprecipitation, leading to a colour transition from green to red and accumulation of reddish nanoparticles during an aging period. Based on this finding, we hypothesize that Fe(III) ions facilitate and stabilize particle formation through complexation, followed by redox reactions.

The initial bluish-green colour with peak visible light absorption at around 620–650 nm may indicate complexation occurring between thiols and Fe(III) ions, as suggested by previous studies.[46,47] Subsequently, during the ensuing aging period, Fe(III) ions might catalyse thiol oxidation, leading to the formation of less water-soluble species through intermolecular disulphide linkages.[48] Notably, the oxidation hypothesis gains support from the detection of Fe(II) ions in the dialysate removed through dialysis (Fig. S16, ESI†). Upon purification, the final nanoparticles exhibit a characteristic red hue,

implying complexation of Fe(II) with the sulphur moieties within the nano-assembly.[48] However, ICP-MS analysis only detected a minute quantity of iron species (0.18 ppm) in the final nanoparticle preparation, in contrast to a significantly higher sulphur content (26.6 ppm) measured. This finding is consistent with the EDS result (Fig. S10, ESI†). The complexation hypothesis could be further substantiated through LC-MS methods or by isolating and characterizing the metal complexes formed in the system.[49,50] Nevertheless, we acknowledge the limitations and challenges of the current study, particularly concerning the transformation of amino acids into pigmented molecules, which, as mentioned above, are yet to be fully understood.

Conclusions

This paper introduces an innovative nanoparticle platform based on our discovery of synergistic browning involving two amino acids within a solvent system. Previously, we demonstrated that a single amino acid, tryptophan, undergoes significant browning in a DMSO/acetone cosolvent system.[16,17] In our present study, we initiated a comprehensive investigation to explore whether binary combinations of amino acids could yield a broader spectrum of browning reactions. To our surprise, we found that several pairs of amino acids exhibited synergistic

6418 | J. Mater. Chem. B, 2024, **12**, 6410–6423

This journal is © The Royal Society of Chemistry 2024

browning effects. Consequently, we set out to harness this new-found amino acid reaction to develop a nano-platform with potential biomedical applications.

We demonstrate that by controlling the synergistic browning of cysteine and lysine in the DMSO/acetone cosolvent system (the organic phase reaction), hydrophobic browning species self-assemble into particles upon mixing the organic phase with water (a solvent-shifting process). The introduction of Fe(III) ions into the water phase facilitates the particle assembly process, resulting in the formation of stable nano-sized particles.

We developed the nanoparticle platform through systematic and thorough optimization across various stages, starting from the browning reaction, followed by nanoprecipitation, aging, and finally, purification. The final nanoparticle preparation consists of spherical nanoparticles measuring 100–200 nm in size, bearing three functional groups, including thiol, carboxylate, and amine. As such, it is a zwitterionic nanoparticle with pH-dependent charge reversal capability. Furthermore, we demonstrate that our nanoparticle preparation possesses a mild antioxidant capacity and can be considered a new type of nano-antioxidant. In conclusion, an innovative nano-platform has emerged from novel amino acid reactions, with great potential for applications in drug delivery and beyond.

Experimental

Materials

Lysine ($\geq$98%, HPLC), cysteine ($\geq$98%, HPLC), and arginine ($\geq$98%, HPLC) were obtained from Sigma-Aldrich. All other amino acids were purchased from ACROS Organics. The following reagents were also from Sigma-Aldrich: iron(III) chloride hexahydrate, ammonium iron(II) sulphate hexahydrate, sodium hydroxide, sodium acetate, 2,2′-azino-bis(3-ethylbenzothiazoline-6-sulfonic acid) diammonium salt (ABTS), 1,1-diphenyl-2-picrylhydrazine (DPPH), 3-(2-pyridyl)-5,6-diphenyl-1,2,4-triazine-4′,4″-disulfonic acid sodium salt (ferrozine), and 2,4,6-tris(2-pyridyl)-s-triazine (TPTZ). The following solvents and reagents were from J.T. Baker: dimethyl sulfoxide, ethanol, methanol, and hydrochloric acid. Potassium persulfate was from the Showa Chemical Industry. Acetone and ascorbic acid were obtained from Honeywell. All chemicals were used as received from vendors without further purification. Deionized water was used throughout, using the ELGA PURELAB Ultra water purification system.

Assessing browning potential in 190 binary amino acid combinations

All possible pairwise combinations of the 20 common amino acids were initially evaluated for their browning capability in a mixture of DMSO and acetone (with a volume ratio of 9/1). A stock solution of each amino acid was prepared at 5 mg mL^{-1} in the solvent mixture, followed by pairwise mixing an equal volume of the 20 amino acid stock solutions. The resulting solutions were left undisturbed at room temperature for 48 hours. Photographs of all 190 combinations, as well as each individual stock solution, were taken and then compared in a tabulated symmetric triangular matrix (20 × 20).

Synergistic browning between the cysteine–lysine pair and between the cysteine–arginine pair

A stock solution of cysteine was prepared at a concentration of 2.5 mg mL^{-1} in a mixture of DMSO and acetone with a volume ratio of DMSO to acetone at 9:1. Stock solutions of lysine and arginine were prepared at 10 mg mL^{-1}, in the solvent mixture. After subjecting all the stock solutions to 2 min of ultrasonic treatment, followed by magnetic stirring at 600 rpm for 5 h, the lysine and arginine stock solutions were further diluted using the same solvent mixture to achieve diluted amino acid solutions at concentrations of 5, 2.5, 1.25, 0.625, 0.312, and 0.156 mg mL^{-1}. Subsequently, 2 mL of the cysteine stock solution was combined with 2 mL of each of the diluted lysine or arginine solutions in 4-mL glass vials. These mixed amino acid solutions were allowed to stand at room temperature for up to 7 days. UV-vis spectra were recorded for the day-7 solutions after appropriately diluting with the blank solvent mixture, using a UV-vis spectrophotometer (Biochrom, Ultrospec 8000pc). The recorded absorbance values were adjusted for the dilution factor and plotted on the same graph. Three independent experiments were conducted, and typical UV-vis spectra were plotted and compared.

Effect of cysteine concentration variation on amino acid browning synergism

The effect of changing cysteine concentrations on the enhancement of amino acid browning was further investigated using the same experimental protocol as outlined above, with the following modifications. The stock solution of cysteine was prepared at a concentration of 10 mg mL^{-1}, while each stock solution of lysine and arginine was prepared at 2.5 mg mL^{-1}. After diluting the cysteine stock solution to concentrations of 5, 2.5, 1.25, 0.625, 0.312, and 0.156 mg mL^{-1}, 2 mL of each of the diluted cysteine solutions were mixed with 2 mL of the stock solution of lysine and arginine, respectively. All other procedures and measurements remained consistent with the previous experiments.

Exploring the nanoparticle preparation conditions

Nanoparticle preparation was conducted via a nanoprecipitation procedure, where nanoparticles were generated by mixing an organic phase with a water phase. The cysteine–lysine pair was selected for its superior predictability in producing synergistic browning. The general process involved the reaction of these two amino acids in an organic phase comprising DMSO and acetone at a volume ratio of 9:1. The preparation of stock amino acid solutions followed the same procedure outlined in the previous sections. Notably, due to the low solubility of both amino acids, especially lysine, in DMSO and acetone, the mixed amino acid solution may contain some undissolved amino acids. Accordingly, the reaction systems were nearly saturated with amino acids. All reactions in the organic phase were performed at room temperature without mechanical stirring. After reaching a certain degree

This journal is © The Royal Society of Chemistry 2024

J. Mater. Chem. B, 2024, 12, 6410–6423 | 6419

of browning in the organic phase at a fixed reaction time, the browning organic phase was filtered through filter paper to separate the undissolved amino acids. Subsequently, the filtrate was carefully added dropwise into a water phase, with the total preparation volume maintained at 1 mL. The preparation conditions were systematically explored and optimized by adjusting various parameters, including (1) the ratio of the organic phase to the water phase, (2) browning duration, (3) concentrations of amino acids in the organic phase, (4) concentrations of ferric chloride in the water phase, and (5) aging time. The resulting particle dispersions, before or after centrifugation and redispersion, were initially analysed for particle size distribution using dynamic light scattering (Zetasizer Nano ZS90, Malvern, UK). Furthermore, time-dependent changes of dispersion's spectroscopic properties were measured using a multimode microplate reader (Spark 10M, TECAN, Austria).

Scaling-up and optimizing the aging and particle collection process (the 10-mL reaction protocol)

After conducting rapid and systematic investigations into the initial conditions for particle preparation (*i.e.*, a 1-mL reaction), the next step involved optimizing the aging and particle collection/purification process with a tenfold increase in the total reaction volume (*i.e.*, a 10-mL reaction). The detailed preparation procedures are as follows: dissolve 100 mg of cysteine in 5 mL of the organic phase, consisting of 4.5 mL of DMSO and 0.5 mL of acetone, while stirring magnetically at 600 rpm for 5 h. Separately, dissolve 50 mg of lysine in 5 mL of the same solvent mixture. Combine 5 mL of each amino acid stock solution to create a 10-mL reaction mixture. Subject the mixing solution to ultrasonic treatment for 2 min, followed by allowing the solution to stand for 7 days at room temperature. After 7 days of browning, filter the browning organic phase to obtain the organic phase filtrate. Prepare a water phase containing 0.625% (w/v) ferric chloride hexahydrate, equivalent to 23.1 mM ferric ions. Slowly and dropwise add 2 mL of the organic phase filtrate into 8 mL of the water phase within 30 s, following magnetic stirring at 300 rpm for 30 s. Remove the stir bar. For aging at room temperature, allow the resulting particle dispersion to stand undisturbed at room temperature up to 7 days. For aging at elevated temperatures, incubate the resulting particle dispersion in a water bath for 24 h, setting the incubation temperature at 40 and 60 °C, respectively. To purify and collect nanoparticles, at a pre-specified aging time point, transfer the particle dispersion to a dialysis bag (with a molecular weight cut-off (MWCO) of 12–14 kDa, Spectral Por, Thomas Scientific, USA) and place it in a 2 L external dilute HCl solution at pH 3. Allow continuous dialysis for 24 h, replacing the old external solution at 1, 2, 4, and 6 h with fresh solution.

Dynamic light scattering (DLS), transmission electron microscopy (TEM), scanning electron microscopy (SEM), and energy dispersive X-ray spectroscopy (EDS)

The hydrodynamic sizes of nanoparticles were determined through DLS measurements using the Zetasizer Nano ZS90 (Malvern, UK). The reported data include the mean particle sizes, the polydispersity index (PDI), and the particle size distribution profile.

The nanoparticles were examined through transmission electron microscopy (TEM) and scanning electron microscopy (SEM). For the TEM analysis, a 2.5 µL sample was deposited onto formvar-coated and carbon-coated copper grids (product number 71150, Electron Microscopy Sciences, USA) and left to dry in a desiccator. TEM images were captured using a JEM-2000EXII (JEOL, Japan).

In the case of SEM analysis, samples were placed and allowed to dry on copper specimen stubs. SEM images were acquired using a JSM-7600F (JEOL, Japan). The SEM samples were further subjected to energy dispersive X-ray spectroscopic analysis (EDS; Oxford Aztec X-Max80).

Electrochemical properties

The zeta potentials of the finally purified nanoparticle preparations, obtained from the 10-mL reaction protocol, were measured at various pH levels. The sample was purified and obtained through dialysis against an external solution with a pH of 3. Subsequently, the pH of the sample solution was adjusted by adding incremental amounts of 0.1 N NaOH, covering a pH range from 3 to 10. Zeta potentials and hydrodynamic diameters were determined using the Zetasizer Nano ZS90 (Malvern, UK). The experiments were replicated three times using independent batches of samples. The hydrodynamic size and zeta potential data were plotted against the mean pH values corresponding to the amount of NaOH added to the sample.

Fourier transform infrared (FTIR) analysis

The purified nanoparticle samples, obtained from the 10-mL reaction protocol, were frozen at −80 °C and then underwent a 24-h freeze-drying process to remove water content. The FTIR spectra of the resulting lyophilized sample powder were collected using an IR-Affinity-1S (Shimadzu, Japan).

X-ray photoelectron spectroscopy (XPS) analysis

The lyophilized sample powder was affixed to conductive copper tape. XPS analysis was performed at ULVAC-PHI, Quantera II, using an X-ray source operating at 1486.6 eV. Surface chemical compositions were examined through both survey (wide) scans (224 eV per step 0.8 eV) and narrow scans (55 eV per step 0.1 eV) of carbon (C), oxygen (O), nitrogen (N), and sulphur (S). This analysis was outsourced to an external contract service provided by Integrated Service Technology (iST). Other instrumental parameters included the X-ray source (a scanning X-ray microprobe with an Al anode), X-ray beam size (200 µm, 50 W), correction of the carbon charging effect (284.8 eV), imaging resolution (<10 µm), angle-resolved analysis (45°), analysis time (20 minutes), and spectrum de-convolution software (Multipak).

Inductively coupled plasma mass spectrometry (ICP-MS) analysis

The fully digested nanoparticle solution, which had undergone an 8-h heating process in a 1 : 3 (v/v) mixture of nitric acid and

6420 | *J. Mater. Chem. B*, 2024, **12**, 6410–6423

This journal is © The Royal Society of Chemistry 2024

hydrochloric acid, was used for analysis. The diluted sample solution was analysed for iron and sulphur contents using an iCAP TQ instrument (Thermo Scientific, Germany). This analysis was carried out through an outsourced service provided by the Instrumentation Center at National Tsing Hua University. The detection limits for iron and sulphur were 0.0432 ppb and 0.0015 ppb, respectively.

Ferrozine assay

The concentrations of ferrous ions formed during both the particle aging period and dialysis were measured using the ferrozine assay. The browning reaction was carried out for the cysteine–lysine pair at concentrations of 10 mg mL^{-1} and 5 mg mL^{-1}, respectively, in a DMSO/acetone mixture with a 9 : 1 (v/v) ratio. After allowing the reaction to proceed for 7 days at room temperature, 0.2 mL of the organic phase was taken and added into 0.8 mL of water containing 23.1 mM ferric ions. The resulting solution was aged in a water bath at 60 °C. For the ferrozine assay, the sample was withdrawn from the aging solution and diluted 200-fold. Then, 50 μL of the diluted sample solution was mixed with 50 μL of assay buffer (70 mM sodium acetate buffer) and 50 μL of ferrozine solution (1 mM in water). After allowing the reaction to proceed for 5 min, the absorbance at 562 nm was measured using a spectrophotometric reader (Spark 10 M TECAN, Austria). The concentrations of ferrous ions were determined using a standard curve constructed with ammonium iron(II) sulphate hexahydrate. To determine the dialyzable amount of ferrous ions, the same assay protocol was applied to the samples obtained from the external solution of the dialysis system.

Physical stability during storage

The nanoparticle dispersions were stored in a 4 °C freezer for a duration of 30 days. At pre-determined intervals, samples were investigated to monitor potential changes in particle sizes using DLS.

Antioxidative activities

The antioxidative potential of the final nanoparticle preparations was evaluated through three different assays, specifically the DPPH, ABTS, and FRAP assays. The particle samples were prepared and purified following the 10-mL reaction protocol (Section 4.6). Initial particle concentrations (w/v) were determined through a calibrated procedure that involved weighing the dried sample with an ultrasensitive balance (with a sensitivity of 0.1 mg). Each assay was replicated three times using samples from 3 independent batches, spanning 6 concentration levels ranging from 0.03 mg mL^{-1} to 0.13 mg mL^{-1}.

DPPH assay

The assay solution was prepared by dissolving 1,1-diphenyl-2-picrylhydrazine (DPPH) in 95% alcohol, resulting in a concentration of 400 μM. The free radical scavenging reaction was initiated by mixing 0.3 mL of the diluted sample solutions with 0.3 mL of the assay solution. After allowing the reaction to proceed for 30 min at room temperature in the dark, the mixture underwent centrifugation at 21 130 rcf for 10 min.

Subsequently, 100 μL of the supernatant was measured within a visible light wavelength range from 400 to 800 nm. The characteristic absorption peak at 520 nm was recorded for the calculation of free radical scavenging activity (%), as follows.

$$\text{Scavenging activity}\,(\%) = \frac{A_c - (A_s - A_b)}{A_c} \times 100$$

where A_c, A_s, and A_b represent the absorbances of the control (without particles), sample (with particles), and blank (without DPPH) solutions, respectively.

ABTS assay

The assay solution was prepared by dissolving the 2,2′-azino-bis 3-ethylbenzothiazoline-6-sulfonic diammonium salt (ABTS) (7 mM) in an aqueous solution of potassium persulfate (2.45 mM). Following storage at room temperature in the dark, for 12 to 16 h, the assay solution was obtained by appropriate dilution, achieving an absorbance value of 1.40 ± 0.02 at 734 nm. The assay was conducted by mixing the sample solution with the assay solution in equal volumes of 50 μL within a well of a 96-well plate. The absorbance of the reaction mixture was measured after 300 min at 734 nm (denoted as A_s). The measurement also included blank (without ABTS, A_b) and control solutions (without nanoparticles, A_c). The calculation of free radical scavenging activity was performed using the same equation as outlined above.

FRAP (ferric reducing antioxidant power) assay

The assay solution consists of 2,4,6-tris(2-pyridyl)-s-triazine (TPTZ) and ferric chloride in an acetate buffer at pH 3.6. To prepare it, start by preparing a 2.5 mL TPTZ solution (10 mM) in a 40 mM HCl solution and a 2.5 mL ferric chloride solution (20 mM) in water. Next, mix the TPTZ and ferric chloride solutions with 25 mL of 100 mM acetate buffer (pH 3.6), placing the mixture in a water bath at 40 °C for 10 min to obtain the final assay solution. The assay was performed by mixing 100 μL of the sample solution with 900 μL of the assay solution in a centrifuge tube. A blank solution was prepared by substituting the assay solution with water. After allowing the solutions to stand in the dark for 30 min, they were centrifuged at 21 130 rcf for 10 min. Take 100 μL of the resulting supernatant and measure its absorbance at 593 nm. The blank-corrected absorbance was then used to estimate the vitamin C equivalent antioxidant capacity through the construction of a vitamin C standard curve.

Cytotoxicity

HCT-116 cells, a human colorectal cancer cell line obtained from the Bioresource Collection and Research Center (BCRC), were cultured in Dulbecco's Modified Eagle Medium (DMEM, D5648, Sigma-Aldrich) supplemented with 10% fetal bovine serum (FBS, 35-010-CV, Corning). Cells were maintained in a controlled, humidified environment with 5% CO_2 at 37 °C. For the cell viability assay, cells were seeded in 96-well microplates at densities of 15 000, 6000, and 4000 cells per well, with incubation periods of 24, 48, and 72 h, respectively. After 24 h

of incubation and removal of the culture medium, cells were treated with 200 μL of serially diluted nanoparticle solutions in the culture medium. The nanoparticle-treated cells were further incubated for the specified time intervals. Viable cells were measured using the MTT assay. In wells where the particle solutions were removed, 100 μL of a 0.5 mg mL^{-1} MTT solution was added, and the microplate was then placed in the incubator for 3 h. After removing the MTT solution, formazan crystals formed in each well were dissolved in 100 μL of DMSO. Following 30 s of shaking the microplate, the absorbance at 570 nm was measured using a spectrophotometer (Spark 10M, TECAN, Austria).

Nucleic acid delivery potential

The capability of the nanoparticles to entrap nucleic acids was evaluated using G3139 as a model nucleic acid. G3139 (5′-TCTCCCAGCGTGCGCCAT-3′) is an 18-mer phosphorothioate oligodeoxynucleotide obtained from Alpha DNA (Montreal, Canada). The nanoparticle preparations underwent centrifugation at 10 000 rcf for 10 min. Following the removal of the supernatant, the nanoparticle pellets were redispersed in a pH 3 dilute HCl solution. The entrapment experiment involved mixing 1 mL of nanoparticle dispersions with 10 μL of G3139 at various concentrations dissolved in water. After 30-min incubation, the mixture underwent centrifugation at 30 000 rcf for 10 min, and the UV absorbance at 260 nm (NanoDrop) was measured in the supernatant to estimate the remaining nucleic acid concentrations. The entrapment efficiency was then calculated by subtracting the measured concentration from the added concentration and dividing by the added concentration to obtain the percentage. The nanoparticle–G3139 complex was further characterized for changes in hydrodynamic particle sizes.

Author contributions

TM Hu: conceptualization, methodology, resources, writing – original draft preparation, writing – reviewing and editing, visualization, project administration, supervision, funding acquisition; JA Liang: investigation, formal analysis, visualization, validation; and YH Chiang: investigation, visualization.

Conflicts of interest

There are no conflicts to declare.

Acknowledgements

Notes and references

1 X. Hou, T. Zaks, R. Langer and Y. Dong, *Nat. Rev. Mater.*, 2021, **6**, 1078–1094.

2 R. Tenchov, R. Bird, A. E. Curtze and Q. Zhou, *ACS Nano*, 2021, **15**, 16982–17015.

3 L. Xu, X. Wang, Y. Liu, G. Yang, R. J. Falconer and C.-X. Zhao, *Adv. NanoBiomed Res.*, 2022, **2**, 2100109.

4 M. Jeong, Y. Lee, J. Park, H. Jung and H. Lee, *Adv. Drug Delivery Rev.*, 2023, 114990.

5 S. S. Gupta, V. Mishra, M. D. Mukherjee, P. Saini and K. R. Ranjan, *Int. J. Biol. Macromol.*, 2021, **188**, 542–567.

6 M. N. Leiske and K. Kempe, *Macromol. Rapid Commun.*, 2022, **43**, 2100615.

7 H. Ren, L. Wu, L. Tan, Y. Bao, Y. Ma, Y. Jin and Q. Zou, *Beilstein J. Nanotechnol.*, 2021, **12**, 1140–1150.

8 Q. Zou and X. Yan, *Chem. – Eur. J.*, 2018, **24**, 755–761.

9 Y. Li, Q. Zou, C. Yuan, S. Li, R. Xing and X. Yan, *Angew. Chem., Int. Ed.*, 2018, **57**, 17084–17088.

10 X.-Q. Zhao, F. Wahid, X.-J. Zhao, F.-P. Wang, T.-F. Wang, Y.-Y. Xie, S.-R. Jia and C. Zhong, *Mater. Lett.*, 2021, **300**, 130161.

11 X. He, L. Yang, H. Su, S. Lin, D. Qi, H. Chen, Y. Qu, L. Liu and X. Feng, *J. Controlled Release*, 2021, **337**, 306–316.

12 A. M. Garcia, R. Lavendomme, S. Kralj, M. Kurbasic, O. Bellotto, M. C. Cringoli, S. Semeraro, A. Bandiera, R. De Zorzi and S. Marchesan, *Chem. – Eur. J.*, 2020, **26**, 1880–1886.

13 P. Xing, S. Z. F. Phua, X. Wei and Y. Zhao, *Adv. Mater.*, 2018, **30**, 1805175.

14 T.-M. Hu, C.-Y. Lin, H.-C. Chou and M.-J. Wu, *J. Colloid Interface Sci.*, 2019, **554**, 166–176.

15 Y.-H. Chiang, M.-J. Wu, W.-C. Hsu and T.-M. Hu, *J. Mater. Chem. B*, 2020, **8**, 8830–8837.

16 T.-M. Hu and Y.-H. Chiang, *Biochem. Biophys. Res. Commun.*, 2021, **536**, 67–72.

17 C.-Y. Huang, H.-W. Liao and T.-M. Hu, *RSC Adv.*, 2023, **13**, 29802–29808.

18 H. Ejima, J. J. Richardson, K. Liang, J. P. Best, M. P. van Koeverden, G. K. Such, J. Cui and F. Caruso, *Science*, 2013, **341**, 154–157.

19 Z. Guo, W. Xie, J. Lu, X. Guo, J. Xu, W. Xu, Y. Chi, N. Takuya, H. Wu and L. Zhao, *J. Mater. Chem. B*, 2021, **9**, 4098–4110.

20 C. Tang, D. Amin, P. B. Messersmith, J. E. Anthony and R. K. Prud'homme, *Langmuir*, 2015, **31**, 3612–3620.

21 C. Pucci, C. Martinelli, D. De Pasquale, M. Battaglini, N. di Leo, A. Degl'Innocenti, M. Belenli Gümüş, F. Drago and G. Ciofani, *ACS Appl. Mater. Interfaces*, 2022, **14**, 15927–15941.

22 W. Xu, Z. Lin, S. Pan, J. Chen, T. Wang, C. Cortez-Jugo and F. Caruso, *Angew. Chem., Int. Ed.*, 2023, **62**, e202312925.

23 Y. Guo, Q. Sun, F.-G. Wu, Y. Dai and X. Chen, *Adv. Mater.*, 2021, **33**, 2007356.

24 L. Li, L. Liao, Y. Ding and H. Zeng, *RSC Adv.*, 2017, **7**, 10361–10368.

25 S. Devi, B. Singh, A. Paul and S. Tyagi, *Anal. Methods*, 2016, **8**, 4398–4405.

26 H. Cui, J. Yu, Y. Zhai, L. Feng, P. Chen, K. Hayat, Y. Xu, X. Zhang and C.-T. Ho, *Trends Food Sci. Technol.*, 2021, **115**, 391–408.

27 K. P. García, K. Zarschler, L. Barbaro, J. A. Barreto, W. O'Malley, L. Spiccia, H. Stephan and B. Graham, *Small*, 2014, **10**, 2516–2529.

6422 | *J. Mater. Chem. B*, 2024, **12**, 6410–6423

This journal is © The Royal Society of Chemistry 2024

28 H. Ou, T. Cheng, Y. Zhang, J. Liu, Y. Ding, J. Zhen, W. Shen, Y. Xu, W. Yang and P. Niu, *Acta Biomater.*, 2018, **65**, 339–348.

29 Q. Li, C. Wen, J. Yang, X. Zhou, Y. Zhu, J. Zheng, G. Cheng, J. Bai, T. Xu and J. Ji, *Chem. Rev.*, 2022, **122**, 17073–17154.

30 Y. Y. Yuan, C. Q. Mao, X. J. Du, J. Z. Du, F. Wang and J. Wang, *Adv. Mater.*, 2012, **24**, 5476–5480.

31 F. Veider, E. Sanchez Armengol and A. Bernkop-Schnürch, *Small*, 2023, 2304713.

32 J. Wu, Y. Zheng, M. Liu, W. Shan, Z. Zhang and Y. Huang, *ACS Appl. Mater. Interfaces*, 2018, **10**, 9916–9928.

33 Y. Hirai, R. Saeki, F. Song, H. Koide, N. Fukata, K. Tomita, N. Maeda, N. Oku and T. Asai, *Int. J. Pharm.*, 2020, **585**, 119479.

34 C. A. Stein, S. Wu, A. M. Voskresenskiy, J. F. Zhou, J. Shin, P. Miller, N. Souleimanian and L. Benimetskaya, *Clin. Cancer Res.*, 2009, **15**, 2797–2807.

35 M. Murata, *Glycoconjugate J.*, 2021, **38**, 283–292.

36 F. Hayase, Y. Takahashi, S. Tominaga, M. Miura, T. Gomyo and H. Kato, *Biosci., Biotechnol., Biochem.*, 1999, **63**, 1512–1514.

37 J. M. Ames, A. Apriyantono and A. Arnoldi, *Food Chem.*, 1993, **46**, 121–127.

38 J. M. Ames, R. G. Bailey and J. Mann, *J. Agric. Food Chem.*, 1999, **47**, 438–443.

39 T. Hofmann, *Helv. Chim. Acta*, 1997, **80**, 1843–1856.

40 T. Hofmann, *Carbohydr. Res.*, 1998, **313**, 203–213.

41 S. Sasaki, Y. Shirahashi, K. Nishiyama, H. Watanabe and F. Hayase, *Biosci., Biotechnol., Biochem.*, 2006, **70**, 2529–2531.

42 F. Hayase, T. Usui and H. Watanabe, *Mol. Nutr. Food Res.*, 2006, **50**, 1171–1179.

43 Y. Shirahashi, H. Watanabe and F. Hayase, *Biosci., Biotechnol., Biochem.*, 2009, **73**, 2287–2292.

44 T. Hofmann and S. Heuberger, *Z. Lebensm*, 1999, **208**, 17–26.

45 O. Frank and T. Hofmann, *J. Agric. Food Chem.*, 2000, **48**, 6303–6311.

46 F. Page, *Trans. Faraday Soc.*, 1955, **51**, 919–925.

47 M. Sisley and R. Jordan, *Inorg. Chem.*, 1995, **34**, 6015–6023.

48 M. Y. Hamed, J. Silver and M. T. Wilson, *Inorg. Chim. Acta*, 1983, **80**, 237–244.

49 M. E. Caetano-Silva, M. T. Bertoldo-Pacheco, A. F. Paes-Leme and F. M. Netto, *Food Res. Int.*, 2015, **71**, 132–139.

50 I. B. O'Loughlin, P. M. Kelly, B. A. Murray, R. J. FitzGerald and A. Brodkorb, *J. Agric. Food Chem.*, 2015, **63**, 2708–2714.

This journal is © The Royal Society of Chemistry 2024

J. Mater. Chem. B, 2024, **12**, 6410–6423 | **6423**